Highly Porous Materials as Tunable Electrocatalysts for the Hydrogen and Oxygen Evolution Reaction

*Marc Ledendecker, Guylhaine Clavel, Markus Antonietti, and Menny Shalom**

The facile preparation of highly porous, manganese doped, sponge-like nickel materials by salt melt synthesis embedded into nitrogen doped carbon for electrocatalytic applications is shown. The incorporation of manganese into the porous structure enhances the nickel catalyst's activity for the hydrogen evolution reaction in alkaline solution. The best catalyst demonstrates low onset overpotential (0.15 V) for the hydrogen evolution reaction along with high current densities at higher potentials. In addition, the possibility to alter the electrocatalytic properties of the materials from the hydrogen to oxygen evolution reaction by simple surface oxidation is shown. The surface area increases up to 1200 m^2g^{-1} after mild oxidation accompanied by the formation of nickel oxide on the surface. A detailed analysis shows a synergetic effect of the oxide formation and the material's surface area on the catalytic performance in the oxygen evolution reaction. In addition, the synthesis of cobalt doped sponge-like nickel materials is also delineated, demonstrating the generality of the synthesis. The facile salt melt synthesis of such highly porous metal based materials opens new possibilities for the fabrication of diverse electrode nanostructures for electrochemical applications.

1. Introduction

Electrochemical water splitting to hydrogen (HER) and oxygen (OER) in alkaline solution plays a growing role in the fabrication of alternative energy devices due to the need of clean and sustainable energy.[1] The catalysts should demonstrate low overpotentials towards the wanted reaction, alongside with reasonable current densities. Up to now, for the hydrogen side ($2H_2O + 2e^- \rightarrow H_2 + 2OH$- in alkaline media), platinum is the best catalyst, showing high cathodic current densities at negligible overpotential.[2] However, the performance of many catalysts is reduced in alkaline compared to acid medium due to the initial water dissociation step.[3,4] Albeit platinum shows almost perfect behavior for the HER, the drawback lies in the comparatively low abundance and the thus resulting high price. Though, new structured Pt materials with high surface area have been reported recently by different approaches.[5]

M. Ledendecker, Dr. G. Clavel, Prof. Dr. M. Antonietti, Dr. M. Shalom
Max-Planck Institute of Colloids and Interfaces
Department of Colloid Chemistry
14476, Potsdam, Germany
E-mail: Menny.Shalom@mpikg.mpg.de

DOI: 10.1002/adfm.201402078

Contrarily, the OER ($4OH^- \rightarrow O_2 + 4e^- + 2H_2O$ in alkaline media) is more complicated due to the high number of steps involved. As in the HER, the best catalysts for the OER consist on less abundant and expensive materials such as RuO_2 or IrO_2. Additionally, IrO_2 suffers from poor long term stability in alkaline solution.[6] Alternatives comprising more abundant and cheap materials as cobalt (Co),[7] nickel (Ni),[8,9] iron (Fe),[10] manganese (Mn),[11] their alloys (Ni–Co, Ni–Fe, Ni–Mo), oxides,[12] nitrides and carbides have been subject of intense research due to their promising electrocatalytic properties. For example, Ni based materials are considered to be one of the most efficient non-noble electrocatalysts in alkaline solution. Moreover, modifications (i.e., alloying and doping) of Ni and nickel oxide based materials can result in higher activity, both for HER and OER.[13]

One way to increase the catalytic behavior of these metals is by insertion of foreign dopants into materials possessing high surface areas.[14] Very recently, we showed the possibility to prepare highly porous Ni sponge materials embedded into amorphous C/N layers by means of a molten salt synthesis route. In general, the synthesis is considered relatively easy and safe, and a great variety of porous materials with respect to pore size distribution and surface area can be obtained.[15] Thereby, the salt can either act as the reaction medium (being inert to the desired reaction) or participate actively in the reaction. Careful design of the synthesis (salt melt composition, heating temperature, organic source, etc.) allows to tune the composition along with the chemical and the catalytic properties of the resulting material.

Here we present a facile method to fabricate highly active manganese doped nickel-sponge materials for electrocatalytic applications (HER and OER). The effect of the manganese concentration on the chemical and the electrochemical properties is carefully studied. Moreover, we show that mild oxidation of these materials increases the surface area and alters the electrochemical activity. The composition, morphology and surface area of the resulting manganese doped nickel materials were characterized by X-ray diffraction (XRD), scanning electron microscopy (SEM), high-resolution transmission electron microscopy (HRTEM), high angle annular dark field- scanning transmission electron microscopy (HAADF-STEM), energy dispersive X-ray spectroscopy (EDX), inductively coupled plasma atomic emission spectroscopy (ICP-OES), thermo gravimetric

analysis (TGA), nitrogen sorption measurements and elemental analysis (EA). The electrochemical activity was broadly evaluated by cyclic voltammetry (CV), linear sweep voltammetry (LSV) and chronovoltammetry measurements in alkaline solution.

2. Results and Discussion

2.1. Characterization Studies

Drawing upon the aforementioned synthesis, a route for manganese doping into the sponge-like structures was developed. Shortly, the synthesis is based on simple mixing and heating of nickel chloride ($NiCl_2$), manganese chloride ($MnCl_2$), lithium chloride (LiCl) and dicyanodiamide (DCDA) as organic precursor (Table S1, Supporting Information (SI)). The sample names are constructed in the form of A_xB_y with x and y as index indicating the molar ratio of the specific metal (A and B) in the starting reaction mixtures.

Among these three salts, $NiCl_2$ possesses the highest melting point at 1030 °C, followed by $MnCl_2$ at 650 °C and LiCl at 610 °C.[16] Together, they form a salt melt with reduced melting point depending on the salt ratio. For example, standard reaction mixtures of $LiCl_2$ and $NiCl_2$ in a 2:1 ratio melt down at 800 °C. The mixture was heated up to 800 °C, in which the reaction proceeds in a salt flux process where metal ion dissolution takes place. Thereby, the metal ions react with the amorphous C/N layer. The porogenic effect of the salt melt can be evaluated by comparing surface areas before and after template removal (Figure S1, SI). After salt removal, the surface area (SA) exceeds more than fifty times the SA of the unwashed sample. Hereby, SAs of almost 1000 m^2/g can be achieved with average pore size diameters in the mesoporous dimensions (Table S2, Figure S2, SI).[17] During the washing process, the salt is liberated from the pores within the remaining C/N/metal matrix.

The diffraction patterns of manganese doped nickel materials using different metal salt ratios are shown in **Figure 1**a. For all samples having a higher $NiCl_2$ amount (>0.1) in the starting

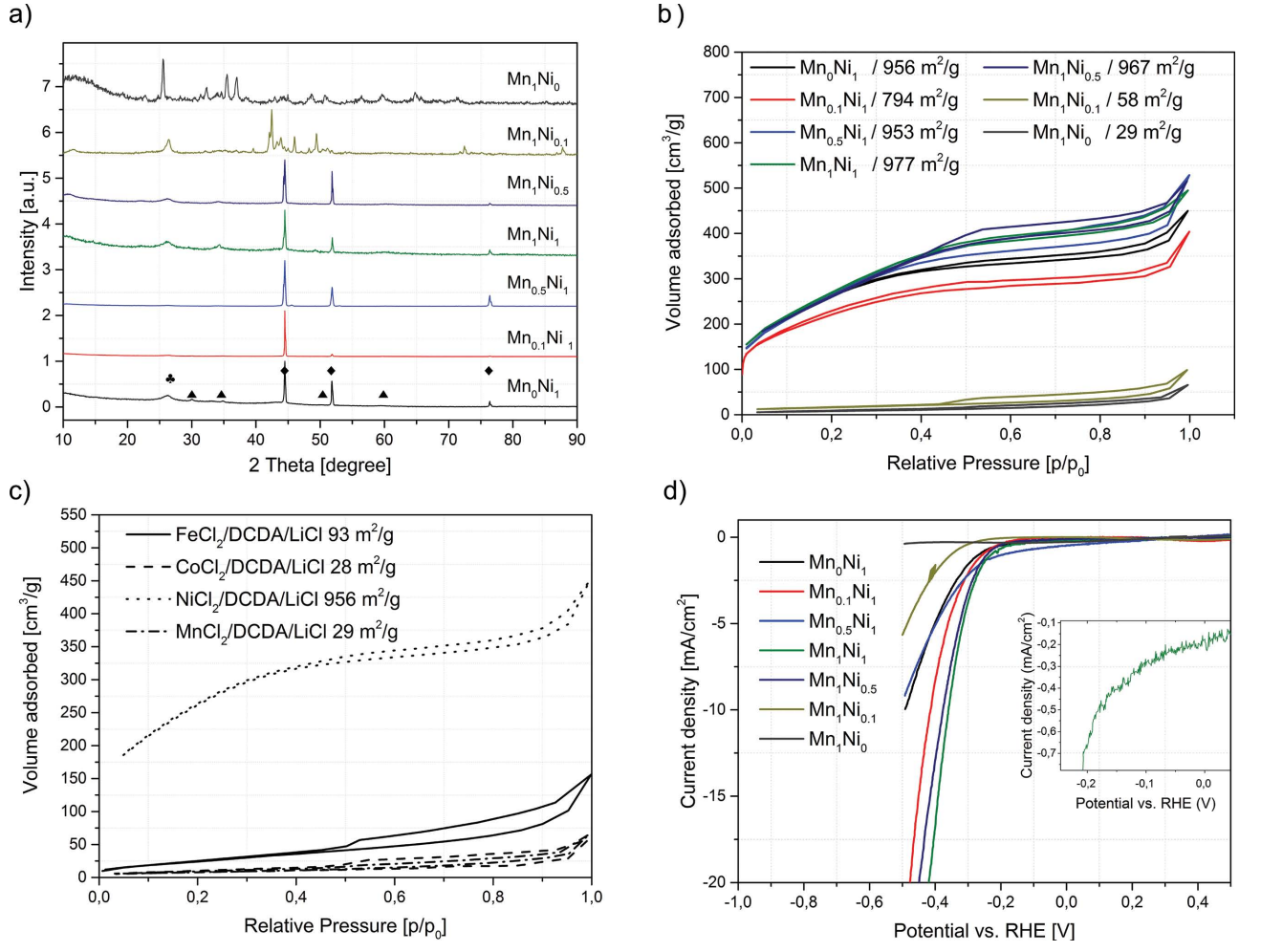

Figure 1. a) XRD patterns of all manganese doped materials (♣ indicating graphitic (002; ICDD 04–016–0554), ♦ Ni (111, 200, 220; ICDD: 04–016–4761) and ▲ LiCl (111, 200, 220, 311; ICDD: 04–015–1302) diffraction peaks. b) Nitrogen sorption isotherms and the corresponding surface areas of Mn_XNi_Y materials and c) the resulting materials from different metal chlorides precursors. d) Polarization curves for all samples in 0.1 M KOH at 400 rpm. Inset: LSV for Mn_1Ni_1 demonstrating a low onset overpotential of 0.15 V.

Table 1. EA (C and N) and ICP-OES (Ni, Mn) data of various materials synthesized in a salt melt process.

Sample	C [wt%]	N [wt%]	Mn [wt%]	Ni [wt %]
Mn_0Ni_1	40	5	–	19
$Mn_{0.1}Ni_1$	39	3	0.6	22
$Mn_{0.5}Ni_1$	37	5	0.8	18
Mn_1Ni_1	40	4	1.6	19
$Mn_1Ni_{0.5}$	35	4	1.8	21
$Mn_1Ni_{0.1}$	38	2	12	19
Mn_1Ni_0	10	7	20	–

materials, only cubic metallic Ni pattern are observed while lower amounts or in absence of Ni, the XRD patterns show mixtures of Mn_xO_y along with unidentified peaks (no metallic Mn was detected). Development of double peaks shifted to smaller angels could be observed when comparing the characteristic nickel peaks (111, 200, 220) when different manganese amounts were added (Figure S3, SI). Assumable, manganese can be incorporated into the cubic nickel structure leading to peak shifts as demonstrated before ($Mn_{0.018}Ni_{0.982}$ – ICDD: 04–011–9057, $Mn_{0.22}Ni_{0.78}$ – ICDD: 04–003–2244, $Mn_{0.5}Ni_{0.5}$ – ICDD: 04–004–8458). The easy reduction of Ni^{2+} to Ni^0 compared to the manganese counterpart can be explained by the lower standard reduction potential of Mn compared to Ni.[18] Moreover, ICP-OES measurements clearly show that high $NiCl_2$ to $MnCl_2$ (>0.1) ratios in the starting material leads to low manganese amounts in the final product (≈1–2%, **Table 1**). However, when using a high $MnCl_2$ to $NiCl_2$ ratio, the manganese amount increases to 12 ($Mn_1Ni_{0.1}$) and 20 wt% (Mn_1Ni_0), respectively. In addition, for all samples, graphitic peaks can be observed in the XRD patterns. Moreover, we note that due to the nature of the synthesis, the metal distribution is not fully homogeneous as shown before.[19]

Nitrogen sorption analysis reveals the necessity of $NiCl_2$ in the salt melt process in order to form highly porous materials (Figure 1b, Table S2 (SI)). For all samples, only the nickel based materials (obtained from XRD) exhibit high surface areas while in the absence of nickel, the surface area of the resulting materials remains relatively low. Very interestingly, the same trend (low surface areas in the absence of $NiCl_2$) was observed with other transition metal systems (Figure 1c) as $CoCl_2$/LiCl/DCDA and $FeCl_2$/LiCl/DCDA, probably due to decreased miscibility of the carbon precursor in the metal salt melt as shown before.[15]

While the knowledge regarding the electrochemical properties of nickel alloys and combinations with Co, Fe and Mo is well established, to the best of our knowledge, the influence of manganese doping on nickel in HER performance is not described. Hence, in this paper we mainly focus on the chemical and electrochemical properties of the manganese doped nickel-sponge. The morphology change when using different salt ratios can be clearly observed from the SEM images (Figure S4,S5, SI) The morphology of the resulting material changes significantly from a sponge-like structure (Figure S3, SI) for the Ni-rich materials ($NiCl_2$ > 0.1) to a flower-like structure (Figure S5 (SI), $Mn_1Ni_{0.1}$) when using lower $NiCl_2$ amounts. In the absence of $NiCl_2$ in the starting salts, only primary particles (≈100 nm) can be observed (Figure S5 (SI), Mn_1Ni_0).

2.2. Electrocatalytic Hydrogen Generation

The strong influence of Mn doping into the Ni-superstructure on the electrochemical performance for the HER is shown in Figure 1d. For all materials, manganese doping results in lower overpotentials accompanied by a rampant increase in current density compared to the pure nickel catalyst (Ni_1Mn_0). LSV (**Figure 2**a) of our best catalyst (1.6% Mn, Mn_1Ni_1) shows a small HER onset potential of ≈0.15 V and an overpotential of 0.36 V at 10 mA/cm^2. A summary of recent catalysts and their performances towards the HER can be found in Table S3 (SI).[21, 25-28] One possible explanation of the increased performance when doped with manganese doping could lie in the enhanced dissociation of the H-OH bond at Mn ($H_2O \leftrightarrow H+OH^-+e^-$). After water dissociation, hydrogen can be adsorbed at the nickel surface (Volmer step: $H \leftrightarrow Ni–H_{ad}$) where the recombination to H_2 in a Tafel or Heyrovsky fashion takes place. Figure 2b shows a TEM image elucidating the distribution of metal nanoparticles embedded into the carbon matrix. Thereby, differently orientated lattice fringes give notice to small nanoparticles surrounded by carbon layers. HAADF-STEM reveals the presence of small nanoparticles (brightest area) surrounded by darker carbon and nitrogen layers (Figure 2c). These particles appear much smaller than expected from the XRD spectrum showing relatively sharp nickel peaks leading to the conclusion that small metal particles coexists with bigger, in carbon embedded crystals. Elemental mapping (Figure 2d,e) shows that nickel and manganese appear to be in immediate vicinity, supporting the hypothesis of a facilitated water dissociation step at manganese followed by the recombination of two adjacent hydrogens at Ni. The full EDX spectrum of both mapping materials can be found in Figure S6. Furthermore, EELS (Figure S7, SI) supports elemental analysis and ICP-OES indicating a higher carbon to nitrogen ratio and an excess of nickel in comparison to manganese even though, due to the smaller sample area, the Ni/Mn ratio determined by EELS is more than twice the ratio determined by ICP-OES. Furthermore, the shape of the first carbon peak (287 eV) supports the XRD patterns showing some graphitic layer formation, but mainly amorphous nitrogen doped carbon. The stability of the best catalyst was studied by cyclic voltammetry (before and after 100 cycles) and chronovoltammetry measurements, keeping the current densities higher than 10 mA/cm^2 for two hours (Figure 2a). After 100 cycles, the performance of Mn_1Ni_1 even improves showing higher current density at lower overpotential. In addition, chronovoltammetry measurements show negligible decrease in current density (less than 5% at over 10 mA/cm^2) when keeping the potential constant (0.36 V vs RHE, Figure 2a, inset).

2.3. Material Optimization for the Oxygen Evolution Reaction

As already mentioned, Ni based materials are well known as non-noble metal electrocatalysts for the OER.[8,20,21] In the same manner, our sample which was based only on Ni (without Mn doping) demonstrates relatively similar performance to the ones described in literature (Figure S8).[8] Interestingly, we found that manganese doping decreases the electrochemical activity in OER, speaking for a tighter binding of oxygen along the manganese sites (which was expected). It is also important to note that the OER performance may not only take place at the Ni surface

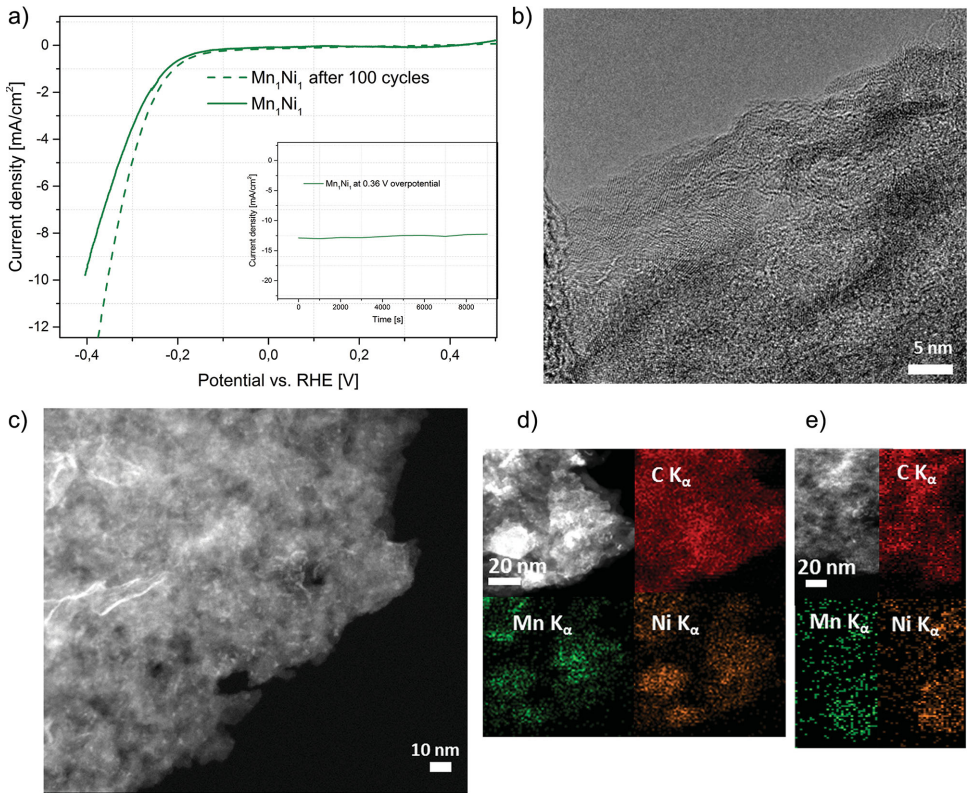

Figure 2. a) Linear sweep voltammetry of Mn_1Ni_1 before and after 100 cycles. The inset shows the chronovoltammetry measurements of Mn_1Ni_1 at 0.36 V overpotential. b) HRTEM images, c) HAADF-STEM, and d,e) EDX mapping of two regions of Mn_1Ni_1. The full EDX spectrum of d and e can be found in the Supporting Information (Figure S5).

but also at the nitrogen doped carbon as described recently by Zhao and co-workers.[22] They hypothesize that the increased performance comes from the readily adsorption of OH^- on the positively charged carbon, favoring the recombination of two adjacent O_{ads} species. All materials were annealed for 10 h under air at 300 °C in order to improve the electrocatalytic activity in the OER. The challenge was to find the right temperature in order to preserve the carbon/nitrogen matrix but activate the nanoparticles inside these layers. In this manner, the temperature was selected according to TGA analysis (Figure S9, SI) showing no material loss at 300 °C. SEM images of all materials before and after 10 h at 300 °C are shown in Figure S4 and Figure S5 (SI), revealing no morphology change after oxidation for 10 h. Hereby, mild annealing probably results in partial oxidation of the nickel and manganese sites to their oxides. The NiO formation can be assessed by the XRD patterns (Figure S10, SI) of the annealed material at 300 °C for 10 h.

Figure 3a and Figure S11 (SI) show the electrocatalytic activity of the modified materials (10 h at 300 °C) in the OER and HER, respectively. Interestingly, the mild oxidation alters the catalytic activity of all materials for the HER and OER. Figure 3b shows a full LSV scan for HER and OER of Mn_1Ni_1 (the best HER catalyst) before and after the thermal modification. This additional activation step drastically enhances the current density (including the slope) along with lowering the overpotential for the OER while the opposite effect occurs on the HER-side. A total voltage efficiency of 70% can be obtained for the water splitting reaction by dividing the theoretical cell potential (1.23 V) by the necessary applied onset potential (1.76 V) of our catalyst on both electrode sides. The decreased HER performance can be explained by the fact that metal oxides favor the cleavage of the H–OH bond but impair the conversion of H_{ad} to H_2.[3,23] For simplification, the influence of the oxidation process is shown only for our most active OER electrocatalyst ($Mn_{0.1}Ni_1$) by material annealing for 3 h, 10 h, and 15 h at 300 °C. The change in material morphology with respect to the annealing time becomes evident from the SEM images (**Figure 4**). The morphology does not change during the oxidation process at lower oxidation times (Figure 4, 0–10 h, 300 °C) in contrast to higher oxidation times (15 h) where more bulk material is obtained. The formation of NiO on the surface is shown in **Figure 5**a, in which characteristic NiO patterns can already be obtained after 10 h. As expected, the crystallite sizes increased while increasing the annealing time (from Scherer equation, $Mn_{0.1}Ni_1$, 15h: ≈15 nm; $Mn_{0.1}Ni_1$ 10 h: ≈5 nm). Moreover, the annealing time strongly influences the surface area of the material (Figure S12, Table S5, SI). Due to the slow condensation of the C/N layer at 300 °C (Table S5, SI), the heating process increases the surface area around 33% with almost no C/N loss. Further heating up to 15 h results in a massive C/N loss, collapse of the supporting scaffold and as a consequence the surface area drops.

The influence of the heating time on the electrochemical activity of the material is shown in Figure 5b. After thermal

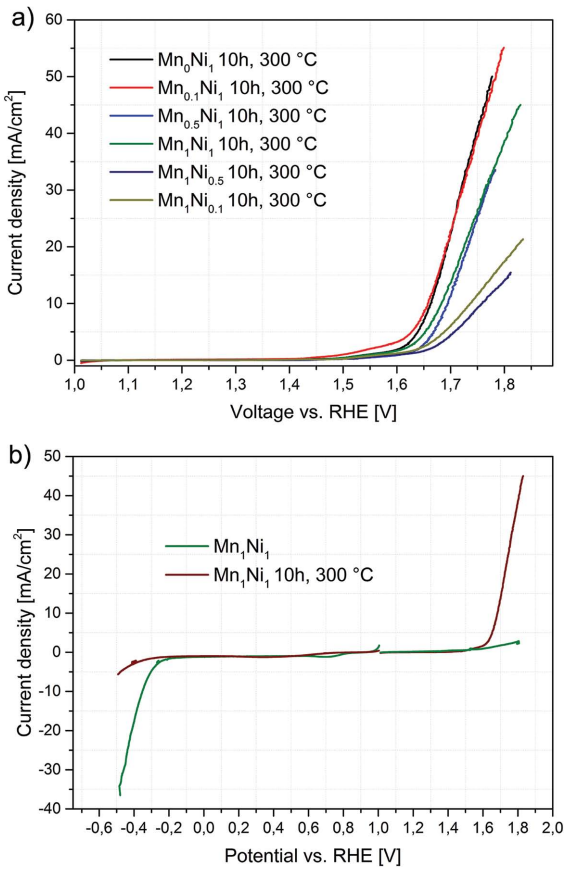

Figure 3. a) Linear sweep voltammetry of all samples activated at 300 °C for 10 h. b) Linear sweep voltammetry of Mn_1Ni_1 before and after surface activation at 300 °C.

treatment for 10 h, the performance of the electrocatalyst is highly improved. The best sample ($Mn_{0.1}Ni_1$, 10 h) exhibits a relative low onset overpotential (0.36 V) along with high current density (10 mA/cm^2 at 0.42 V) which is comparable to the best non-noble electrocatalysts.[24] Additional heating up to 15 h results in the decline of the electrochemical performance, probably due to the massive surface area loss. The influence of surface area and NiO formation on the electrocatalytic properties is shown in Figure 5c. As a result, an increased surface area leads to an improved performance in the OER reaction due to more catalytic active sites. At the same time, the formation of NiO on the surface has to be favored. Hence, $Mn_{0.1}Ni_1$ before and after 15 h annealing exhibits almost the same current density while the surface area decreases by a factor of four. From this data, we can carefully suggest that there is a synergetic effect of both, the surface area and the NiO formation, for the electrocatalytic enhancement in OER.

3. Conclusion

In conclusion, we demonstrated an easy and generic method to synthesize high surface area metal doped nickel materials embedded into nitrogen doped carbon as electrocatalysts for HER and OER. Our results show that the incorporation of manganese into the nickel material enhances the catalyst activity in the HER, with negligible effects on the OER performance. The best HER electrocatalysts demonstrates low overpotentials with relativity high current densities. In addition, we found that the electrochemical properties of Ni-based materials can be altered by simple annealing resulting in the formation of metal oxides on the surface alongside with an increase in surface area. Consequently, after oxidation, the electrocatalysts demonstrate high activity in

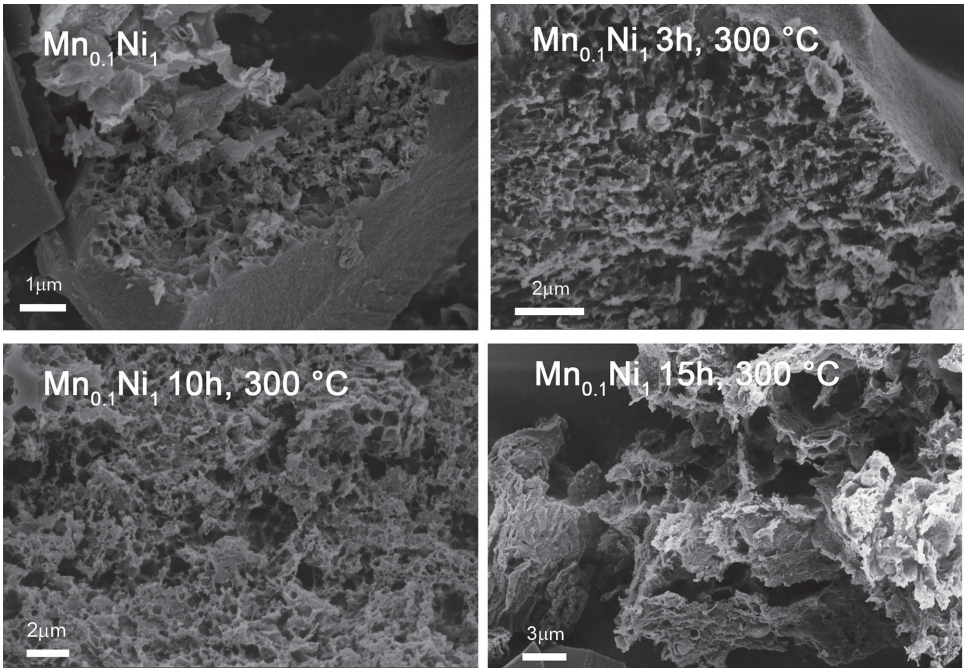

Figure 4. SEM images for $Mn_{0.1}Ni_1$ after different oxidation times at 300 °C.

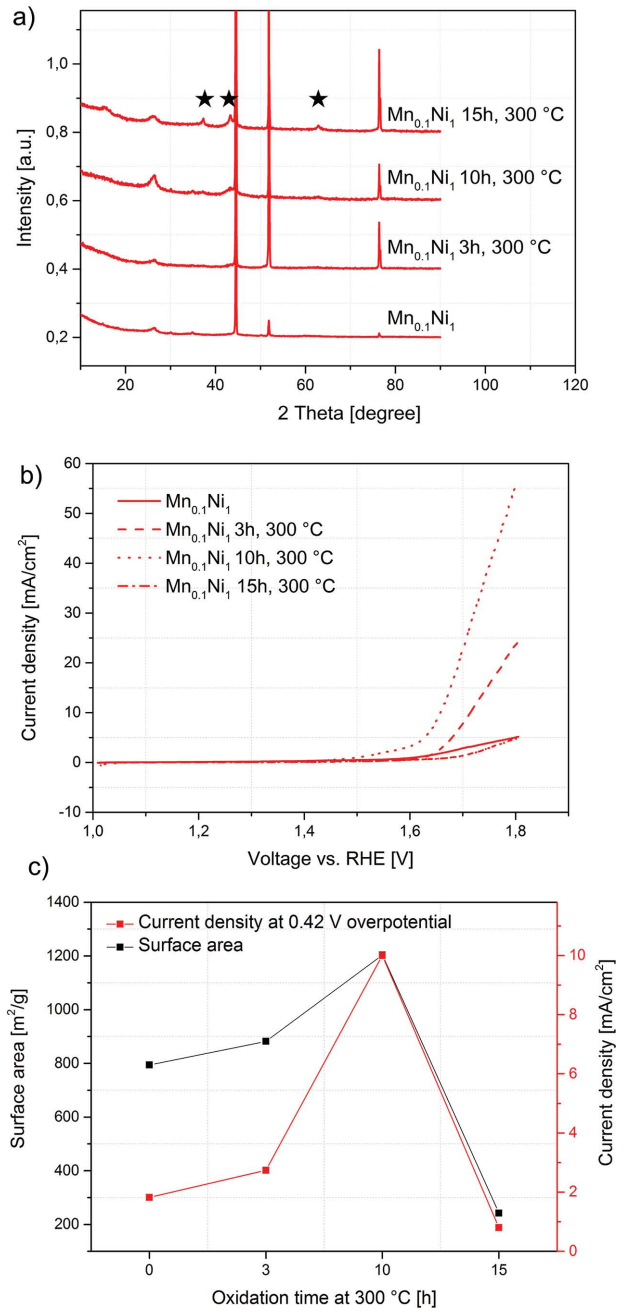

Figure 5. a) XRD patterns of $Mn_{0.1}Ni_1$ after different oxidation times at 300 °C (★ corresponding to NiO (111, 200, 220; ICDD: 04–013–0890) diffraction peaks. b) Linear sweep voltammetry for the oxygen evolution reaction of $Mn_{0.1}Ni_1$ after activation at 300 °C. c) The surface area and the current density at 0.42 V versus RHE as a function of oxidation times.

OER. In sum, the activity of the highly porous material can be easily tuned from HER to OER only by simple thermal treatment in air, leading to a 70% overall water splitting efficiency. We believe that the simple salt melt synthesis together with the effect of the mild oxidation treatments opens new synthesis opportunities of many metal and metal oxide materials for energy related applications.

4. Experimental Section

Synthesis of Porous Materials: The synthesis route was used from Shalom and co-workers[19] and was modified with manganese chloride in the starting materials. Different molar ratios (Table S1, SI) of manganese chloride ($MnCl_2$, Acros), nickel chloride ($NiCl_2$, Aldrich), lithium chloride (LiCl, Roth) and dicyandiamide (DCDA, Aldrich) were mixed together and grinded thoroughly. After mixing, the powders were provided into an alumina crucible and were heated first to 400 °C at a rate of 40 °C min^{-1}, left there for 6 h and heated up afterwards to 800 °C at a rate of 40 °C min^{-1} for 10 h in nitrogen atmosphere. After cooling down to room temperature (RT), the product was grinded thoroughly and washed in milipore water overnight in order to remove the salt excess. After vacuum filtration and washing with water and ethanol, the black powders were dried at 50 °C in vacuo. 3d transition metal doping (Co, Fe) into the nickel-sponge structure could be achieved by using the same synthesis and substituting $MnCl_2$ by $FeCl_2$ or $CoCl_2$. When $NiCl_2$ was exchanged completely by $FeCl_2$ or $CoCl_2$, only small surface areas could be observed. The LiCl and DCDA amount remains the same as shown in Table S4 (SI). The SEM images are shown in Figure S13 (SI). Figure S14 (SI) shows the XRD patterns of Co_1Ni_1 with prominent metallic nickel peaks. ICP-OES measurements of Co_1Ni_1 indicate a Co content of 3.5 wt%. Nitrogen sorption experiments show a low surface area of 244 m^2/g due to the remaining, pore blocking salt content (Figure S15, SI). With the purpose of forming metal oxides on the surface of the carbon material, all samples were heated up in an air oven to 300 °C for 10 h with a rate of 30 °C min^{-1}. In order to get more insights of the oxidizing process, $Mn_{0.1}Ni_1$ (showed the best performance in OER together with Mn_0Ni_1) was selected for further oxidation studies. Thereby, the $Mn_{0.1}Ni_1$ sample was oxidized at 300 °C for different hours (3, 10 and 15 h).

Characterization: For XRD measurements, a Bruker D8 Advance instrument with Cu Ka radiation was used. The pore size distribution was calculated using a quenched solid density functional theory (QSDFT) cylindrical/spherical adsorption kernel. For nitrogen sorption experiments at 77 K, the samples were first degassed for 20 h at 150 °C and then provided to a Quantachrome Quadrasorb Si porosimeter. The Brunauer-Emmet-Teller (BET) model was applied to the isotherms in order to determine the apparent surface area. Thereby, the adsorption branch in the relative pressure range of $p/p_0 < 0.3$ was used for surface area analysis. A SISTA-MPX (Varian) instrument was used for inductively coupled plasma (ICP-OES). The manganese content was measured at wavelengths of 257.61 nm and 259.37 nm whereas the nickel content was measured at 216.55 nm and 231.60 nm respectively. SEM images were acquired by a LEO 1550-Gemini at an acceleration voltage of 5 kV. TEM, STEM, EELS and EDX measurements were performed on a FEI TITAN microscope operated at an acceleration voltage of 300 kV and equipped with a post column EELS spectrometer (GATAN Tridiem). For TEM observation, the samples were dispersed in chloroform and deposited onto holey carbon copper TEM grids.

Electrochemical Measurements: Electrochemical measurements were performed in a three electrode arrangement in 0.1 M KOH. A saturated calomel electrode (SCE) was used as reference electrode. A platinum wire was used as counter electrode. For linear sweep polarization curves, the working electrode was rotated at 400 rpm. HER polarization curves were obtained by potential sweeps from 0 to –1.5 V vs SCE. OER polarization curves were obtained by sweeping the potential from 0 to 0.8 V versus SCE. In both cases a sweep rate of 5 mV/s was used. Prior to every LSV to the reduction or oxidation side, five potential sweeps in the corresponding direction have been performed. All current density values are normalized in respect to the geometrical surface area. The working electrode was prepared by mixing 5 mg of catalyst with 95 µL of Nafion and 350 µL of ethanol. The dispersion was sonicated for 30 min followed by its deposition (5 µL) on the glassy carbon electrode (0.2 cm^2). Finally the samples were dried at 50 °C. All potentials are iR corrected by high frequency AC impedance measurements with frequencies ranging from 0.1 Hz to 1 kHz, where i donates to the current and R to the uncompensated Ohmic electrolyte resistance (≈50 Ω).

Supporting Information

Supporting Information is available from the Wiley Online Library or from the author.

Acknowledgements

M.S. acknowledges "Minerva Fellowship". The Fritz-Haber Institute is acknowledged for the use of the electron microscope.

Received: June 23, 2014
Revised: October 9, 2014
Published online: November 22, 2014

[1] T. R. Cook, D. K. Dogutan, S. Y. Reece, Y. Surendranath, T. S. Teets, D. G. Nocera, *Chem. Rev.* **2010**, *110*, 6474.
[2] a) J. R. McKone, E. L. Warren, M. J. Bierman, S. W. Boettcher, B. S. Brunschwig, N. S. Lewis, H. B. Gray, *Energy Environ. Sci.* **2011**, *4*, 3573; b) H. B. Gray, *Nat. Chem.* **2009**, *1*, 7; c) R. Subbaraman, D. Tripkovic, K.-C. Chang, D. Strmcnik, A. P. Paulikas, P. Hirunsit, M. Chan, J. Greeley, V. Stamenkovic, N. M. Markovic, *Nat. Mater.* **2012**, *11*, 550; d) L. A. Kibler, *Phys. Chem. Chem. Phys.* **2006**, *7*, 985.
[3] R. Subbaraman, D. Tripkovic, D. Strmcnik, K.-C. Chang, M. Uchimura, A. P. Paulikas, V. Stamenkovic, N. M. Markovic, *Science* **2011**, *334*, 1256.
[4] W. Sheng, A. P. Bivens, M. Myint, Z. Zhuang, R. V. Forest, Q. Fang, J. G. Chen, Y. Yan, *Energy Environ. Sci.* **2014**, *7*, 1719.
[5] a) H. Ataee-Esfahani, Y. Nemoto, L. Wang, Y. Yamauchi, *Chem. Commun.* **2011**, *47*, 3885; b) H. Wang, S. Ishihara, K. Ariga, Y. Yamauchi, *J. Am. Chem. Soc.* **2012**, *134*, 10819.
[6] E. Guerrini, H. Chen, S. Trasatti, *J. Solid State Electrochem.* **2007**, *11*, 939.
[7] T.-L. Wee, B. D. Sherman, D. Gust, A. L. Moore, T. A. Moore, Y. Liu, J. C. Scaiano, *J. Am. Chem. Soc.* **2011**, *133*, 16742.
[8] I. J. Godwin, M. E. G. Lyons, *Electrochem. Commun.* **2013**, *32*, 39.
[9] W. Zhou, X.-J. Wu, X. Cao, X. Huang, C. Tan, J. Tian, H. Liu, J. Wang, H. Zhang, *Energy Environ. Sci.* **2013**, *6*, 2921.
[10] a) M. Gong, Y. Li, H. Wang, Y. Liang, J. Z. Wu, J. Zhou, J. Wang, T. Regier, F. Wei, H. Dai, *J. Am. Chem. Soc.* **2013**, *135*, 8452; b) R. L. Doyle, M. E. G. Lyons, *Phys. Chem. Chem. Phys.* **2013**, *15*, 5224.
[11] a) T. Takashima, K. Hashimoto, R. Nakamura, *J. Am. Chem. Soc.* **2011**, *134*, 1519; b) M. S. El-Deab, M. I. Awad, A. M. Mohammad, T. Ohsaka, *Electrochem. Commun.* **2007**, *9*, 2082; c) K. L. Pickrahn, S. W. Park, Y. Gorlin, H.-B.-R. Lee, T. F. Jaramillo, S. F. Bent, *Adv. Energy Mater.* **2012**, *2*, 1269.
[12] X. Li, F. C. Walsh, D. Pletcher, *Phys. Chem. Chem. Phys.* **2011**, *13*, 1162.
[13] a) R. D. L. Smith, M. S. Prévot, R. D. Fagan, S. Trudel, C. P. Berlinguette, *J. Am. Chem. Soc.* **2013**, *135*, 11580; b) L. Trotochaud, J. K. Ranney, K. N. Williams, S. W. Boettcher, *J. Am. Chem. Soc.* **2012**, *134*, 17253.
[14] N. Menzel, E. Ortel, R. Kraehnert, P. Strasser, *Phys. Chem. Chem. Phys.* **2012**, *13*, 1385.
[15] X. Liu, N. Fechler, M. Antonietti, *Chem. Soc. Rev.* **2013**, *42*, 8237.
[16] G. J. Janz, *Molten salts handbook*, Academic Press, New York **1967**.
[17] a) K. C. W. Wu, Y. Yamauchi, *J. Mater. Chem.* **2012**, *22*, 1251; b) K. C. W. Wu, X. Jiang, Y. Yamauchi, *J. Mater. Chem.* **2011**, *21*, 8934; c) Y. Yamauchi, *J. Ceram. Soc. Jpn.* **2013**, *121*, 831.
[18] W. M. Haynes, *Handbook of chemistry and physics*, Taylor & Francis, London **2012**.
[19] M. Shalom, V. Molinari, D. Esposito, G. Clavel, D. Ressnig, C. Giordano, M. Antonietti, *Adv. Mater.* **2014**, *26*, 1272.
[20] M. B. I. Janjua, R. L. Le Roy, *Int. J. Hydrogen Energy* **1985**, *10*, 11.
[21] L. Feng, H. Vrubel, M. Bensimon, X. Hu, *Phys. Chem. Chem. Phys.* **2014**, *16*, 5917.
[22] Y. Zhao, R. Nakamura, K. Kamiya, S. Nakanishi, K. Hashimoto, *Nat. Commun.* **2013**, *4*, 2390.
[23] P. A. Thiel, T. E. Madey, *Surf. Sci. Rep.* **1987**, *7*, 211.
[24] C. C. L. McCrory, S. Jung, J. C. Peters, T. F. Jaramillo, *J. Am. Chem. Soc.* **2013**, *135*, 16977.
[25] T. F. Jaramillo, K. P. Jørgensen, J. Bonde, J. H. Nielsen, S. Horch, I. Chorkendorff, *Science* **2007**, *317*, 100.
[26] J. Kibsgaard, Z. Chen, B. N. Reinecke, T. F. Jaramillo, *Nat. Mater.* **2012**, *11*, 963.
[27] J. Luo, J.-H. Im, M. T. Mayer, M. Schreier, M. K. Nazeeruddin, N.-G. Park, S. D. Tilley, H. J. Fan, M. Grätzel, *Science* **2014**, *345*, 1593.
[28] H. Vrubel, X. Hu, *Angew. Chem. Int. Ed.* **2012**, *51*, 12703.